Impact of topology in causal dynamical triangulations quantum gravity

J. Ambjørn,[1,2,*] Z. Drogosz,[3,†] J. Gizbert-Studnicki,[3,‡] A. Görlich,[1,3,§] J. Jurkiewicz,[3,‖] and D. Nemeth[4,¶]

[1]*The Niels Bohr Institute, Copenhagen University, Blegdamsvej 17, DK-2100 Copenhagen Ø, Denmark*
[2]*IMAPP, Radboud University, Nijmegen PO Box 9010, The Netherlands*
[3]*Institute of Physics, Jagiellonian University, ul. prof. Stanislawa Lojasiewicza 11, PL 30-348 Krakow, Poland*
[4]*Institute of Physics, Eötvös Loránd University, Pázmány Péter sétány 1/A, 1117 Budapest, Hungary*

(Received 23 May 2016; published 8 August 2016)

We investigate the impact of spatial topology in 3 + 1-dimensional causal dynamical triangulations (CDT) by performing numerical simulations with toroidal spatial topology instead of the previously used spherical topology. In the case of spherical spatial topology, we observed in the so-called phase C an average spatial volume distribution $n(t)$ which after a suitable time redefinition could be identified as the spatial volume distribution of the four-sphere. Imposing toroidal spatial topology, we find that the average spatial volume distribution $n(t)$ is constant. By measuring the covariance matrix of spatial volume fluctuations, we determine the form of the effective action. The difference compared to the spherical case is that the effective potential has changed such that it allows a constant average $n(t)$. This is what we observe and this is what one would expect from a minisuperspace GR action, where only the scale factor is kept as dynamical variable. Although no background geometry is put in by hand, the full quantum theory of CDT is also with toroidal spatial toplogy able to identify a classical background geometry around which there are well-defined quantum fluctuations.

DOI: 10.1103/PhysRevD.94.044010

I. INTRODUCTION

Impressive progress in computing power during the last 20 years has made numerical methods an important tool of contemporary theoretical physics. One example is lattice QCD which provides solutions for low-energy problems of strong interactions not tractable by means of analytic or perturbative methods. The progress has also been used in the quest for a theory of quantum gravity, where nonperturbative approaches play an important role. It is well known that gravity cannot be formulated as a perturbative quantum field theory as it is nonrenormalizable [1,2]. However, following Weinberg's asymptotic safety conjecture [3], there is hope that it can be formulated as a predictive theory in a nonperturbative way. The use of functional renormalization group equations have provided some evidence in favor of the asymptotic safety conjecture in the case of gravity [4–10], but since it involves approximations which are difficult to control, it is important to test the asymptotic safety scenario using other methods, and here the lattice models of gravity may play an important role. The starting point is a lattice regularization of the gravity path integral,

$$\mathcal{Z} = \int \mathcal{D}_{\mathcal{M}}[g] e^{iS_{HE}[g]}, \tag{1}$$

where one integrates over geometries, i.e. the equivalence classes of spacetime metrics g with respect to the diffeomorphism group on manifold $\mathcal{M}$, and S_{HE} is a classical gravitational action. To give meaning to the formal expression (1), one can introduce a lattice discretization. The finite lattice spacing a provides a high-energy cutoff, and by taking $a \to 0$, one can in principle approach the continuum limit. Using what is known as dynamical triangulations (DT), one starts out in the Euclidean sector; i.e., the path integral (1) is changed such that one integrates over geometries with Euclidean signature and uses the corresponding Euclidean action ($iS_{HE}[g_L] \to -S_{HE}[g_E]$, where g_L denotes a geometry with Lorentzian signature and g_E denotes a geometry with Euclidean signature). The regularized (Euclidean) path integral is then

$$\mathcal{Z} = \sum_{\mathcal{T}} e^{-S_R[\mathcal{T}]}, \tag{2}$$

where the sum is over (abstract) triangulations $\mathcal{T}$. Thus, each abstract triangulation is viewed as a piecewise linear geometry, where each link is assigned the length a, and S_R is the discretized Hilbert-Einstein action obtained following Regge's method for describing piecewise linear geometries [11]. Such a partition function can be investigated analytically in $d = 2$ dimensions [12–14] and by using numerical Monte Carlo methods when $d \geq 3$ [15–20]. A natural question arises: in the path integral (1) and consequently in the partition function (2), should one only integrate or sum over geometries of some chosen topology or should one also include a summation over various topologies and, if so, which topologies should be taken into

*ambjorn@nbi.dk
†zbigniew.drogosz@uj.edu.pl
‡jakub.gizbert-studnicki@uj.edu.pl
§andrzej.goerlich@uj.edu.pl
‖jerzy.jurkiewicz@uj.edu.pl
¶nemeth.daniel.1992@gmail.com

account? The problem of summing over all possible topologies seems to be ill defined even in two (spacetime) dimensions, where the number of inequivalent geometries increases factorially with the Euler characteristic. As a consequence, the path integral (2) is not even Borel summable, and a theory may have (infinitely) many nonperturbative versions. The situation is even worse in dimension four, where the classification of all possible topologies does not exist (see [21] for a review of all these issues). Therefore, one is forced to restrict the class of admissible spacetime topologies, and usually only one simple topology is taken into account (in DT this was typically a four-sphere S^4).[1] Numerical simulations of DT in spacetime dimension four showed that there exist two distinct phases, none of which resembles the four-dimensional Universe (see [18–20] and more recently [23,24]). The phases are separated by a first-order phase transition [25,26], which makes the possibility of approaching a continuum limit unlikely; however, the authors of Ref. [27] claim that such a possibility exists if bare coupling constants are fine-tuned in a specific way. Simulations using different topologies ($S^3 \times S^1$ and T^4) led to the same results [28], as one would expect since phase transitions usually are associated with bulk properties where global topological constrains are of little importance. It has been conjectured that the first-order transition is associated with large fluctuations of the lattice version of the conformal mode [29].

The causal dynamical triangulation approach (CDT) tries to change the above situation by starting out with a path integral defined for geometries with Lorentzian signature and by assuming that one only integrates over causal geometries (implemented in the strong form of assuming that the geometry is globally hyperbolic), thus allowing the introduction of a global proper-time foliation. Since a topology change of a spatial slice often is associated with causality violation one forbids such changes in CDT and, as a result, the spacetime topology is a product $\mathcal{M} = \Sigma \times I$, where I denotes a (proper-time) interval and Σ the spatial surface. All these concepts are linked to the Lorentzian signature of the geometry. What is unique for CDT (compared to DT) is that even at the discretized level, i.e. even in the regularized path integral, each of these geometries has an analytic continuation to a geometry with Euclidean signature and in the Euclidean regularized path integral (2) we sum over this class of geometries. The restriction is entirely motivated from the Lorentzian starting point. With such a genuine new set of Euclidean geometries there is a chance that the phase diagram of the lattice theory is changed compared to the DT phase diagram. And this is indeed what happens.

In CDT the time direction is distinguished, and the number of (discrete) time steps is kept fixed in numerical simulations. Due to the imposed time foliation, the four-dimensional triangulation is constructed from two types of elementary building blocks, the (4, 1) simplex with 4 vertices on spatial hypersurface in time t and 1 vertex in $t \pm 1$, and the (3, 2) simplex with 3 vertices in t and 2 vertices in $t \pm 1$. The simplices are glued together along their three-dimensional faces, and local curvature is defined by the deficit angle around two-dimensional triangles. Additionally, trajectories are assumed to satisfy the simplicial manifold condition; i.e., every (sub)simplex with a given set of vertex labels appears only once. It is also assumed that lattice spacing in time and spatial directions may be different, which defines the asymmetry parameter α, such that:

$$a_t^2 = \alpha\, a_s^2. \tag{3}$$

The Regge-Einstein-Hilbert action takes the following form [30],

$$S_R = -(\kappa_0 + 6\Delta)N_0 + \kappa_4(N_{(4,1)} + N_{(3,2)}) + \Delta N_{(4,1)}, \tag{4}$$

where $N_{(4,1)}$, $N_{(3,2)}$ and N_0 denote the total number of (4, 1) simplices, (3, 2) simplices and vertices, respectively, while κ_0, Δ and κ_4 are three dimensionless coupling constants dependent on the bare Newton's constant, cosmological constant and the asymmetry parameter α.

In CDT, the topology of spatial hypersurfaces Σ is a choice. The same is the case in classical GR, where the choice of topology will affect the possible classical solutions. Similarly, we can expect the choice of topology of Σ to affect the possible semiclassical solutions of CDT around which the geometry will fluctuate in the quantum theory. In fact, since no background geometry is put into the path integral in CDT, changing spatial topology is a very interesting test of the picture that dynamically an average suitable background geometry is found around which there are relatively small quantum fluctuations. Further, since CDT starts out as a lattice theory (before the lattice spacing is sent to zero), there is even an additional possibility to effectively defy the topology put in by hand, since on the lattice topology is only an approximate concept: while changing topology dynamically in the continuum will often result in infinite derivative terms, on the lattice such terms will be finite, thus allowing a change in topology. This could happen if the entropy of the "wrong" configurations is so large that it overcomes the action barrier for a topology change. The CDT studies performed so far provide an example of this. Until now the computer simulations have been performed with the spatial topology being S^3, while periodic boundary conditions were imposed in the time direction for purely technical reasons. Thus the total topology of spacetime imposed was $\mathcal{M} = S^3 \times S^1$. However, in the so-called phase C (to be described below) the system effectively arranged itself into a geometry of topology $\mathcal{M} = S^4$ (up to lattice artifacts),

[1]Note that DT is formulated in the Euclidean regime and such a choice is compatible with Hartle-Hawking no-boundary proposal [22].

provided time was chosen sufficiently large. This would not be possible for smooth classical solutions. However, once this has happened and one takes the lattice spacing to zero, only the S^4 part will survive. The possibility of such dynamics makes it additionally interesting to change the topology of Σ and study the corresponding CDT system.

The CDT studies with topology choice $\mathcal{M} = S^3 \times S^1$ have led to the discovery of four distinct phases of geometry [31–34], including a physical phase C where a four-dimensional Universe is observed [31,35] with semi-classical features closely resembling de Sitter space [36,37] and quantum fluctuations governed by the minisuperspace action [37,38]. The physical phase C is separated from phase A by a first-order phase transition and seemed to be separated from phase B by a second-order phase transition line [39,40]. The more recent studies showed the existence of a new "bifurcation" phase (D) in between phases C and B [33,34], and most likely the recently discovered C-D phase transition line is second order [41], thus allowing for the possibility of taking continuum limit from within the physically interesting phase C [42,43].

In this work, we investigate the impact of spatial topology change on CDT results. We analyze a system where the spherical topology S^3 is replaced by a toroidal topology $T^3 \equiv S^1 \times S^1 \times S^1$. For technical reasons we still keep time-periodic boundary conditions, and therefore the resulting spacetime topology is $\mathcal{M} = T^3 \times S^1$.[2]

II. SIMULATION DETAILS

The (Wick-rotated) partition function (2) defines a statistical field theory which can be studied by numerical Monte Carlo methods. The idea is to define a Markov chain in the space of all admissible triangulations, where a triangulation $\mathcal{T}$ is generated with probability:

$$\hat{P}(\mathcal{T}) = \frac{1}{\mathcal{Z}} e^{-S_R[\mathcal{T}]}. \tag{5}$$

This can be done by updating triangulations by a series of local Monte Carlo moves. In four-dimensional CDT, one typically uses seven types of moves which are causal (i.e., they preserve both the chosen spatial topology Σ and the global spacetime topology $\mathcal{M} = \Sigma \times S^1$) and ergodic (i.e., any triangulation of topology $\mathcal{M}$ can be obtained from any other triangulation of topology $\mathcal{M}$ by a sequence of moves —more details can be found in [30]). In addition, we require that simplicial manifold conditions be satisfied.

One usually starts the numerical simulation from an arbitrarily chosen simple triangulation $\mathcal{T}_{\text{start}}$, and by performing the moves one evolves the system in Monte Carlo time. The moves are accepted or rejected according to the detailed balance condition which ensures that after a large number of attempted moves (the so-called thermalization period) the system tends toward a stationary state where the probability of generating a triangulation $P(\mathcal{T}) \to \hat{P}(\mathcal{T})$. The 7 moves which were used in numerical simulations for topology $S^3 \times S^1$ preserve the topology and causality, and can be applied to any topology $\Sigma \times S^1$. The missing part is generating an initial triangulation $\mathcal{T}_{\text{start}}$ for the new spatial topology $\Sigma = T^3$.

We start by triangulating a four-dimensional hypercube into 16 simplices using the triangulation method proposed by P. S. Mara [44]. The 4-cube has 16 vertices, which can be seen in the visualization in Fig. 1, and we assume that the blue vertices (labeled 0–7) belong to the spatial Cauchy hypersurface (the 3-cube) in time t and the red vertices (labeled 8–15) belong to the 3-cube in time $t+1$. In the triangulation, one obtains ten simplices with 4 blue vertices and 1 red vertex or vice versa, all together being the (4, 1) simplices:

$$\{0,1,2,4,8\},\quad \{4,8,12,13,14\},\quad \{2,8,10,11,14\},$$
$$\{2,4,6,7,14\},\quad \{1,2,4,7,14\},\quad \{1,8,11,13,14\},$$
$$\{1,8,9,11,13\},\quad \{1,4,5,7,13\},\quad \{1,2,3,7,11\},$$
$$\{7,11,13,14,15\},$$

where the numbers in parentheses are vertex labels. One also obtains six simplices with 3 vertices in one time slice and 2 vertices in another (the (3, 2) simplices), parametrized by

$$\{1,2,4,8,14\},\quad \{1,4,8,13,14\},\quad \{1,2,8,11,14\},$$
$$\{1,4,7,13,14\},\quad \{1,2,7,11,14\},\quad \{1,7,11,13,14\}.$$

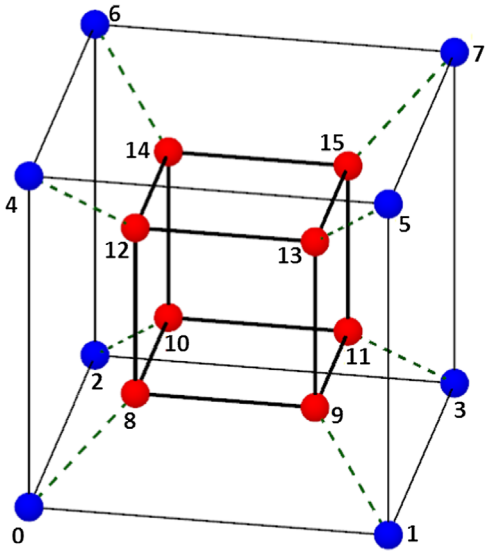

FIG. 1. Visualization of a 4-cube.

[2]Note that the direction of time is still well defined and time is treated differently than space; i.e., we distinguish between spatial Cauchy surfaces and keep the number of time steps fixed. The setup is thus very different from a DT system with $\mathcal{M} = T^4 = S^1 \times S^1 \times S^1 \times S^1$.

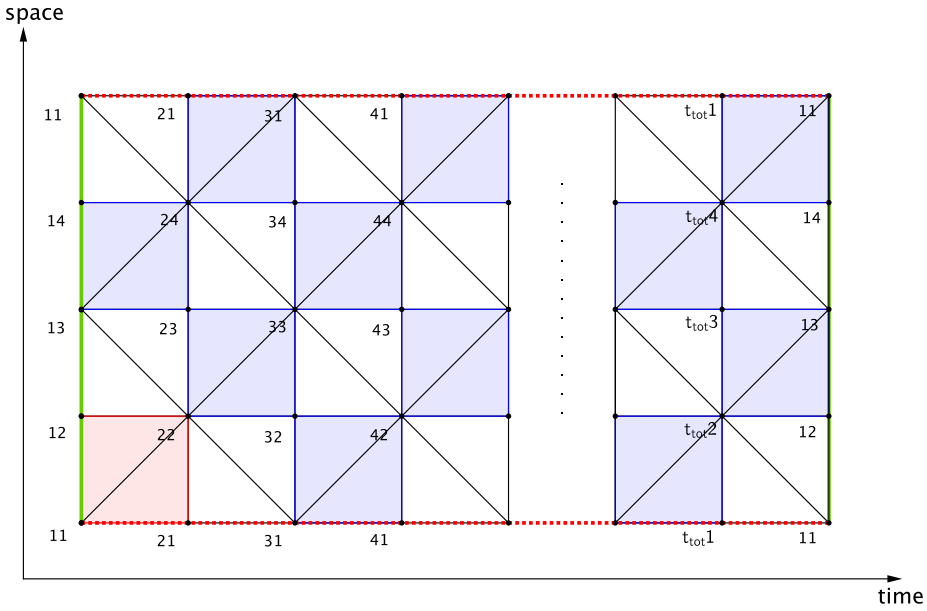

FIG. 2. Two-dimensional visualization of the initial triangulation $\mathcal{T}_{\text{start}}$. The starting cube (square) is colored in red. Colored and blank squares are mirror images of each other. The number of cubes (squares) in spatial direction is 4, and the number in time direction is t_{tot} ($t_{\text{tot}} \geq 4$ and even). The red and green edge lines are glued together, which is done by identifying the corresponding (sub)simplices (vertices and links). Such boundary conditions are consistent with toroidal topology of spatial slices resulting in global topology of $\mathcal{M} = T^1 \times S^1$.

By gluing the hypercubes together in all four directions, we build a four-dimensional initial triangulation $\mathcal{T}_{\text{start}}$, satisfying the regularity constraints. Only those d-dimensional (sub)simplices which share a d-1-dimensional face (d-1 simplex) can be glued together. This can be done by joining together the hypercubes which are mirror images of each other in each direction. As a result, the number of hypercubes in each direction is even.

The configuration must be periodic in all four directions, which can be done by identifying vertex labels of the "last" hypercube in each direction with that of the "initial" hypercube. Additionally, we require that each d-simplex ($d = 0, \ldots, 4$) with vertex labels $\{v_1, \ldots, v_{d+1}\}$ appear only once. To fulfill these requirements, one is forced to use more than two hypercubes in each direction. We use four hypercubes in each spatial direction and t_{tot} hypercubes in the time direction ($t_{\text{tot}} \geq 4$ and even). A simplified two-dimensional visualization of the procedure is presented in Fig. 2. The initial triangulation consists of $64 \cdot t_{\text{tot}}$ 4-cubes containing $1024 \cdot t_{\text{tot}}$ 4-simplices, out of which there are $384 \cdot t_{\text{tot}}$ (3, 2)-simplices and $640 \cdot t_{\text{tot}}$ (4, 1)-simplices. As a result, each spatial slice is initially built from 320 equilateral tetrahedra and has 64 vertices.[3]

It is worth mentioning that the initial triangulation $\mathcal{T}_{\text{start}}$ is not the minimal triangulation, i.e. the one containing the smallest possible number of (sub)simplices, but it is relatively easy to construct. By applying Monte Carlo moves, we managed to shrink the triangulation to the one which has only 90 tetrahedra and 15 vertices in each spatial layer. It seems that the resulting spatial configuration is the smallest possible triangulation of a torus T^3 (by construction the moves do not allow for spatial topology change). We discuss this result in detail in Appendix A. Note that the minimal toroidal triangulation is still much bigger than the minimal spherical configuration from our previous measurements, which consisted of just 5 tetrahedra and had only 5 vertices in each spatial layer. One may, therefore, expect that finite size effects are substantial in current numerical studies.

[3]By construction the number of (4, 1)-simplices is twice the number of spatial tetrahedra. This is because each spatial tetrahedron in time t is a face of one (4, 1) simplex with the fifth vertex in $t + 1$ and one such a simplex with the fifth vertex in $t - 1$.

III. THE RESULTS

In order to study CDT quantum gravity numerically, one needs to define observables whose expectation values or correlation functions can be measured in Monte Carlo simulations. The idea is to probe the space of all possible triangulations with the probability given by (5). As a result, one obtains a sample of triangulations $\{\mathcal{T}_1, \mathcal{T}_2, \ldots, \mathcal{T}_{N_{\text{MC}}}\}$ which can be used to estimate expectation values or correlation functions:

$$\langle \mathcal{O}_1 \ldots \mathcal{O}_n \rangle = \frac{1}{\mathcal{Z}} \sum_{\mathcal{T}} \mathcal{O}_1(\mathcal{T}) \ldots \mathcal{O}_n(\mathcal{T}) e^{-S_R[\mathcal{T}]}$$
$$\approx \frac{1}{N_{\text{MC}}} \sum_{i=1}^{N_{\text{MC}}} \mathcal{O}_1(\mathcal{T}_i) \ldots \mathcal{O}_n(\mathcal{T}_i). \quad (6)$$

One then typically explores the bare couplings parameter space to check how the observables depend on the position in

the parameter space. In principle, various phases can be identified and investigated using this method. For four spacetime dimensions, CDT parameter space is spanned by three bare couplings: κ_0, Δ and κ_4. κ_4 plays the role of the bare cosmological constant, and the leading behaviour of the partition function (2) is

$$Z \propto e^{(\kappa_4^c - \kappa_4)N_4}, \qquad N_4 = N_{(4,1)} + N_{(3,2)},$$

where $\kappa_4^c = \kappa_4^c(\kappa_0, \Delta)$ is a critical value for which the theory becomes exponentially divergent. In numerical simulations, we fix the total number of simplices, which in practice means that we approach a critical value $\kappa_4 - \kappa_4^c \approx 1/N_4$ and thus we are left with a two-dimensional parameter space (κ_0, Δ). One can then check how the observables scale with increasing lattice volume N_4 and thus draw conclusions about the infinite volume limit. In CDT, we typically control the lattice volume by introducing an additional volume fixing potential to the bare action (4). Here we use a quadratic volume fixing term

$$S_{\mathrm{VF}} = \epsilon(N_{(4,1)} - \bar{V}_4)^2 \tag{7}$$

with $\epsilon = 0.00002$ controlling the amplitude of volume oscillations around $\bar{V}_4$.

For the previously used spherical spatial topology the parameter space has been investigated in detail, which led to the discovery of four distinct phases [31–34]. Here, with toroidal spatial topology, we will focus on one particular point in the parameter space, namely ($\kappa_0 = 2.2$, $\Delta = 0.6$), which in the spherical case was placed in the physical de Sitter phase C.[4]

A. Spatial volume profile

An observable investigated in this article is the *spatial volume*:

$$n_t \equiv N_{(4,1)}(t), \tag{8}$$

where $N_{(4,1)}(t)$ is the number of (4, 1) simplices having 4 vertices in time t. This is by construction equal to twice the number of tetrahedra forming a spatial slice in t and, as all spatial tetrahedra are equilateral, the number is proportional to the physical 3-volume of a Cauchy hypersurface in t. In numerical simulations, one can measure the average

$$\bar{n}_t = \langle n_t \rangle, \tag{9}$$

called the volume profile, and the correlator

$$\mathrm{C}_{t,t'} \equiv \langle (n_t - \bar{n}_t)(n_{t'} - \bar{n}_{t'}) \rangle, \tag{10}$$

called the covariance matrix. For the spherical spatial topology, the volume profile observed inside phase C had a blob structure which could be very well fitted with the $\cos^3$ function characteristic for the Euclidean de Sitter solution [36,37] (see Fig. 3, blue line). Now, for the toroidal topology, up to numerical noise, the spatial volume does not depend on t, and consequently the profile is a constant line (see Fig. 3, red line):

$$\bar{n}_t = \bar{v} \equiv \frac{\bar{V}_4}{t_{\mathrm{tot}}}. \tag{11}$$

In order to obtain a better understanding of the difference between $\bar{n}_t$ when $\Sigma = S^3$ and $\Sigma = T^3$, we will determine the effective action as a function of n_t. In the S^3 case, this effective action was closely related to the classical minisuperspace action where only the scale factor of the universe was kept as a dynamical variable.

B. The effective action

The partition function (2) of CDT can be rewritten in the following form:

$$\mathcal{Z} = \sum_{\mathcal{T}} e^{-S_R[\mathcal{T}]} = \sum_{\{n_t\}} \sum_{\mathcal{T}_{\{n_t\}}} e^{-S_R[\mathcal{T}_{\{n_t\}}]}, \tag{12}$$

where the first sum on the right is over (all possible) spatial volume configurations $\{n_t\} \equiv (n_1, n_2, \ldots, n_{t_{\mathrm{tot}}})$, and the second sum is over the subset of all triangulations consistent with the spatial volume configuration $\mathcal{T}_{\{n_t\}}$, i.e. where $\forall t\colon N_{(4,1)}(t) = n_t$. By performing the sum $\sum_{\mathcal{T}_{\{n_t\}}}$ on the rhs of (12) we obtain an effective action depending only on $\{n_t\}$:

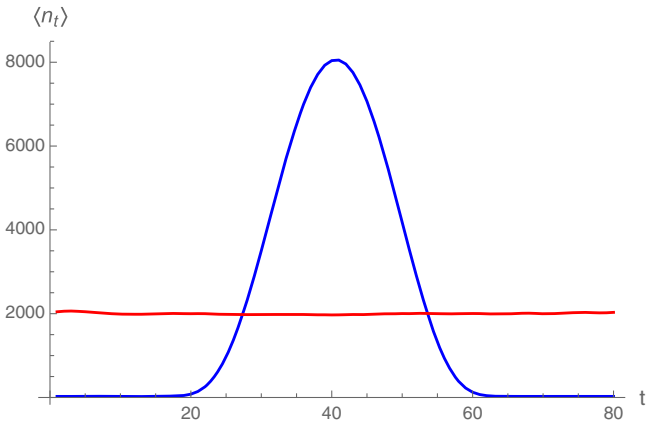

FIG. 3. The spatial volume profile $\langle n_t \rangle$ measured for the toroidal (red line) and spherical (blue line) spatial topology, respectively. Data measured for ($\kappa_0 = 2.2$, $\Delta = 0.6$).

[4]For the toroidal case we investigated several points (κ_0, Δ) of the bare parameter space located inside each of the previously discovered (spherical case) phases: A, B, C and D. Preliminary results show that similar phases may exist in new topological conditions; however, it is not easy to distinguish them by using the methods discussed here. One should also note that finite size effects are much stronger than for the spherical case, and thus one has to simulate with much higher lattice volumes to observe the differences. The results for other points in the parameter space will be discussed elsewhere.

$$\mathcal{Z} = \sum_{\{n_t\}} e^{-S_{\rm eff}[n_t]}, \tag{13}$$

This is a minisuperspace theory of the scale factor ($a(t) \propto n(t)^{1/3}$), but contrary to the ordinary minisuperspace theory it is exact, since we have integrated out the other degrees of freedom rather than just dropping them. *A priori* it is not clear that $S_{\rm eff}[n_t]$ is useful. It could be very nonlocal. However, that turned out not to be the case when the spatial topology was S^3. Measurements showed that $S_{\rm eff}[n_t]$ could be described by a kinetic term and a potential which were closely related to the terms in the original Hartle-Hawking minisuperspace model. Further, the measured minisuperspace action described (up to the numerical uncertainty inherited in the simulations) both the semiclassically observed background $\bar{n}_t$ and the quantum fluctuations of n_t around this background. We will now employ the same methods as used for S^3 to determine the effective action when the space topology is T^3. First we observe that the quantum fluctuations around $\bar{n}_t$ are relatively small. Thus it makes sense to expand $S_{\rm eff}[n_t]$:

$$\begin{aligned} S_{\rm eff}[n_t] &= S_{\rm eff}[\bar{n}_t + \delta n_t] \\ &= S_{\rm eff}[\bar{n}_t] + \delta n_t \frac{\partial^2 S_{\rm eff}}{\partial n_t \partial n_{t'}}\bigg|_{\bar{n}_t} \delta n_{t'} + o[\delta n_t^3] \end{aligned} \tag{14}$$

and the effective propagator is given by the (inverse) covariance matrix

$$\frac{\partial^2 S_{\rm eff}}{\partial n_t \partial n_{t'}}\bigg|_{\bar{n}_t} = C^{-1}_{t,t'}. \tag{15}$$

Hence the covariance matrix measurement enables us to verify any conjectured form of the effective action. Based on the form of the effective action when topology of space is S^3, we make the following ansatz,

$$S_{\rm eff} = \sum_t \left(\frac{(n_t - n_{t+1})^2}{\Gamma(n_t + n_{t+1} - 2n_0)} + V[n_t] \right), \tag{16}$$

where Γ and n_0 are constants. We call the first term the kinetic term and the term $V[n_t]$ the potential. The constant volume profile (11) $\bar{n}_t = \bar{v}$ and the ansatz (16) imply that the inverse covariance matrix should have a simple tridiagonal form[5]

$$C^{-1} = \begin{pmatrix} 2k+u & -k & 0 & \cdots & 0 & -k \\ -k & 2k+u & -k & 0 & \cdots & 0 \\ 0 & -k & 2k+u & -k & \ddots & \vdots \\ \vdots & \ddots & \ddots & \ddots & \ddots & -k \\ -k & 0 & 0 & \cdots & -k & 2k+u \end{pmatrix},$$

with constant diagonal and sub- or superdiagonal elements defined by the kinetic and potential coefficients k and u, respectively,

$$k = \frac{1}{\Gamma(\bar{v} - n_0)}, \qquad u = V''[\bar{v}]. \tag{17}$$

The covariance matrices measured for the point ($\kappa_0 = 2.2$, $\Delta = 0.6$) are indeed consistent with this structure—see Fig. 4, where we show the data measured for $\bar{V}_4 = 160000$ and $t_{\rm tot} = 80$ giving $\bar{v} = 2000$. In order to verify if numerical errors are under control, we used two independent procedures for determining the coefficients k and u. In the first method, we simply invert the measured covariance matrix, and take the average of diagonal or sub- or superdiagonal elements:

$$k = -\langle C^{-1}_{t,t+1} \rangle_t, \qquad u = \langle C^{-1}_{t,t} \rangle_t - 2k. \tag{18}$$

Accordingly, the method can be called "first invert then average." In the second procedure, we assume that due to a uniform spatial volume distribution (n_t independent of t), the real dependence of the covariance matrix is on $\Delta t = t - t'$ and not on t. As a result, $\forall t$ the matrix elements $C_{t,t+\Delta t}$ are identical up to numerical noise. Based on this assumption, we calculate the "averaged" covariance matrix $\bar{C}_{t,t+\Delta t} \equiv \langle C_{t,t+\Delta t} \rangle_t$ (see Fig. 5) and then invert it. By construction we get constant (independent on t) diagonal and sub- or superdiagonal elements, resulting in

$$k = -\bar{C}^{-1}_{t,t+1} = \text{const}, \qquad u = \bar{C}^{-1}_{t,t} - 2k = \text{const}. \tag{19}$$

Therefore, the method can be called "first average then invert." We checked that the results of both methods are very consistent—see Fig. 4, where the blue dashed line and the red line corresponding to the two methods cannot be optically distinguished, and also Figs. 6 and 7, where blue and red dots are obtained by using the two methods, respectively.

In order to check the dependence on $\bar{v}$ and thus verify whether the denominator of the kinetic term in Eq. (16) is linear and find the shape of the potential part, one is forced to use a collection of lattice volumes $\bar{V}_4$ and time periods $t_{\rm tot}$. The results of such an analysis are shown in Figs. 6 and 7, where we present the measurements for all combinations of $\bar{V}_4 = 80000$, 160000, 240000 and $t_{\rm tot} = 10$, 40, 160, 200, resulting in 12 different values of $\bar{v}$. For a consistency check, this also includes $\bar{v} = 2000$, which is identical to the previously discussed case ($\bar{V}_4 = 160000$;

[5]Here we already subtracted the impact of the volume fixing potential (7) which causes a shift of all inverse covariance matrix elements by a constant 2ϵ. The volume fixing shift is also subtracted from the measured (inverse) covariance matrix data.

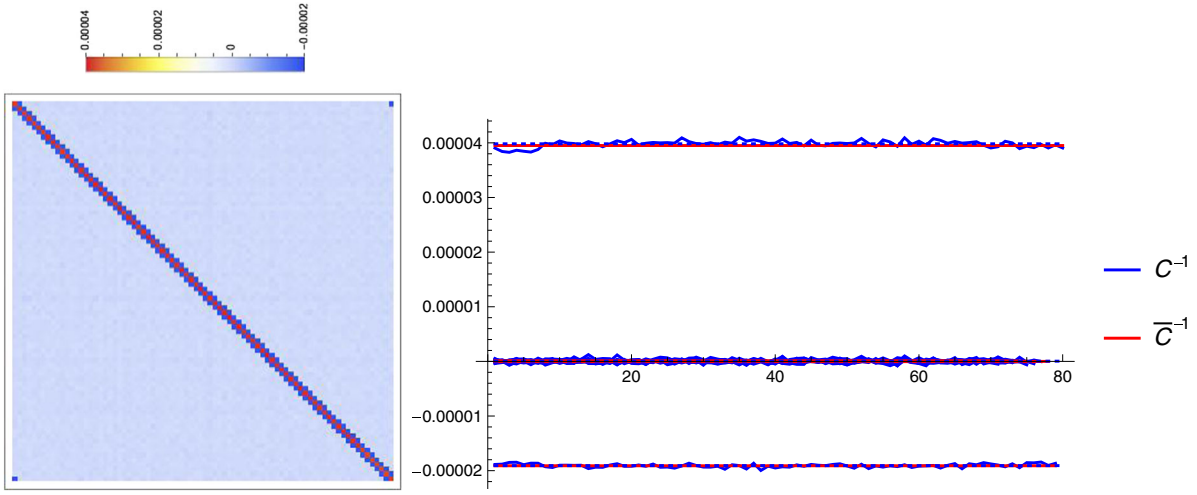

FIG. 4. Left: The inverse covariance matrix C^{-1} measured for ($\kappa_0 = 2.2$, $\Delta = 0.6$), $\bar{V}_4 = 160000$ and $t_{\mathrm{tot}} = 80$. The structure is consistent with the assumed form of the effective action (16). Right: The inverse covariance matrix diagonal (positive), sub- or superdiagonal (negative) and other matrix elements (close to zero). The C^{-1} matrix elements are plotted as blue solid lines and the blue dashed lines are the averages (obtained by the "first invert then average" method described in the text). The red lines are matrix elements obtained by using the method "first average then invert" as described in the text. The results of the two methods are very similar and cannot be optically distinguished.

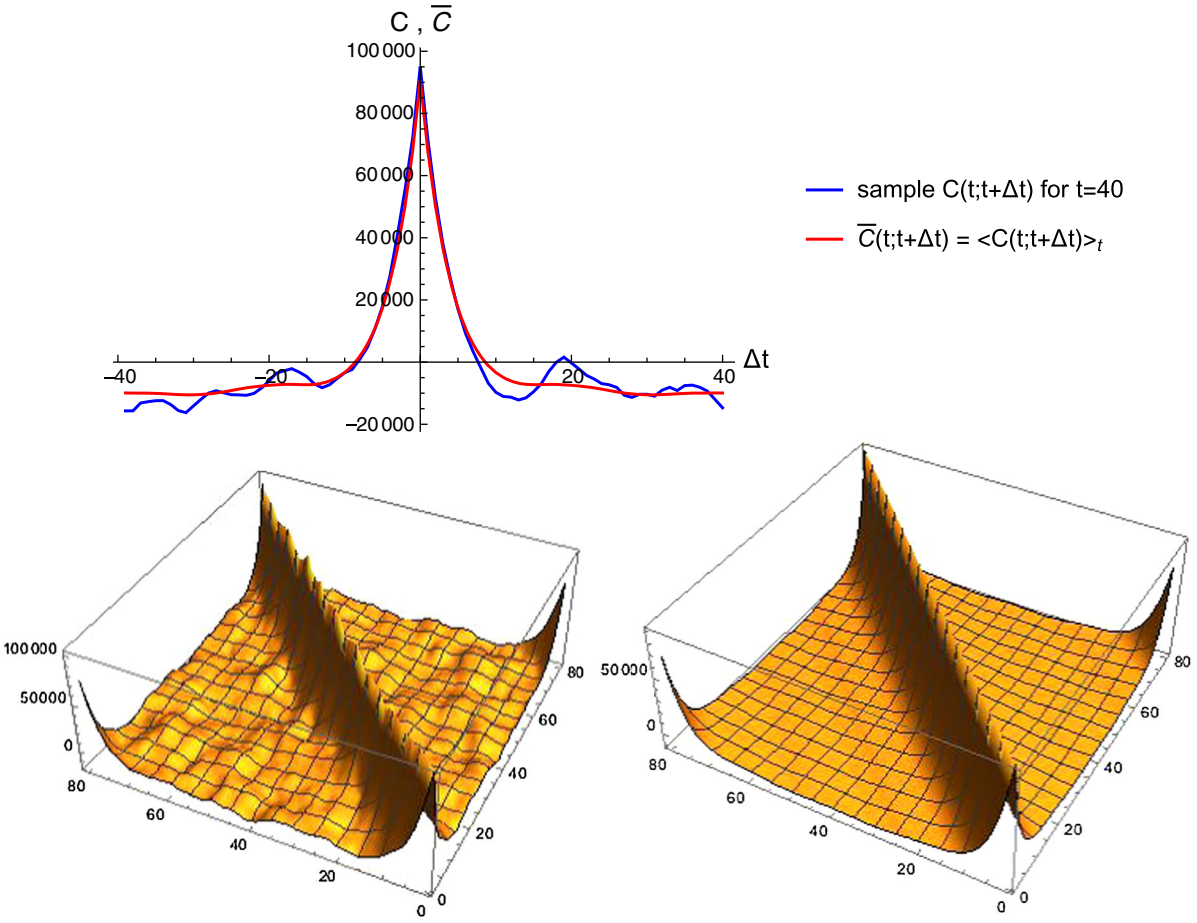

FIG. 5. Illustration of the procedure "first average then invert" described in the text. The upper chart presents a sample row ($t = 40$) of the measured covariance matrix $C_{t,t'}$ plotted as a function of $\Delta t = t - t'$ (blue line) and the "averaged" covariance matrix $\bar{C}_{t,t+\Delta t} \equiv \langle C_{t,t+\Delta t} \rangle_t$ (red line). The lower chart presents the covariance matrix before (left) and after (right) applying the averaging procedure.

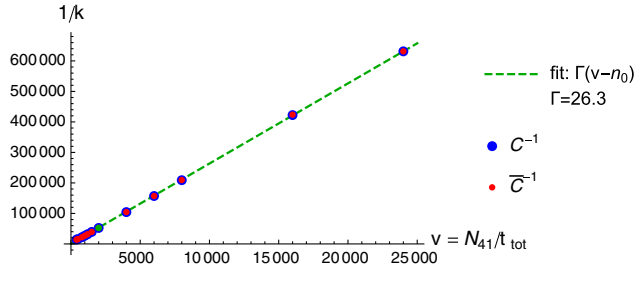

FIG. 6. The (inverse) kinetic coefficients $k = -C^{-1}_{t,t+1}$ as a function of $\bar{v} = \bar{V}_4/t_{\text{tot}}$ obtained for a collection of 12 measurements with $\bar{V}_4 = 80000$, 160000, 240000 and $t_{\text{tot}} = 10$, 40, 160, 200. The linear relation is consistent with Eq. (17) and thus the ansatz (16). Blue points were obtained by applying the procedure "first invert then average," and red points by the procedure "first average then invert," described in the text. The results of the two methods are (almost) identical. Green dots are the results obtained for $\bar{V}_4 = 160000$, $t_{\text{tot}} = 80$ and thus $\bar{v} = 2000$. The dots are indistinguishable from the results for $\bar{V}_4 = 80000$, $t_{\text{tot}} = 40$ resulting in the same $\bar{v} = 2000$.

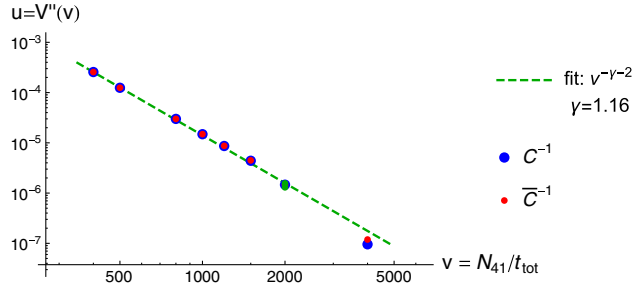

FIG. 7. The potential coefficients $u = C^{-1}_{t,t} - 2k$ as a function of $\bar{v} = \bar{V}_4/t_{\text{tot}}$ obtained for a collection of 12 measurements with $\bar{V}_4 = 80000$, 160000, 240000 and $t_{\text{tot}} = 10$, 40, 160, 200 (data for $\bar{v} > 5000$ were skipped as they were indistinguishable from numeric noise). The plot is in the log-log scale and the dashed line is consistent with a potential $V[\bar{v}] = \mu\bar{v}^{-\gamma}$—see Eq. (17)—and the best fit is for $\gamma = 1.16 \pm 0.02$. Blue points were obtained by applying the procedure "first invert then average," and red points by the procedure "first average then invert." The results of the two methods are (almost) identical. Green dots are the results obtained for $\bar{V}_4 = 160000$, $t_{\text{tot}} = 80$ and thus $\bar{v} = 2000$. The dots are indistinguishable from the results for $\bar{V}_4 = 80000$, $t_{\text{tot}} = 40$ resulting in the same $\bar{v} = 2000$.

$t_{\text{tot}} = 80$). We checked that the k and u coefficients measured for such $\bar{v}$ do not depend on the particular choice of $(\bar{V}_4; t_{\text{tot}})$ (green points in Figs. 6 and 7).

The results obtained for various $\bar{v}$ show that the (inverse) kinetic coefficients k^{-1} are indeed consistent with the expected linear behavior $\Gamma(\bar{v} - n_0)$, and that the best fit of the potential coefficients of form $u[\bar{v}] = \mu(\gamma^2 + \gamma)\bar{v}^{-\gamma-2}$ gives $\mu > 0$ and $\gamma = 1.16 \pm 0.02$, resulting in the following form of the effective action consistent with ansatz (16)[6]:

$$S_{\text{eff}} = \sum_t \left(\frac{(n_t - n_{t+1})^2}{\Gamma(n_t + n_{t+1} - 2n_0)} + \mu n_t^{-\gamma} + \lambda n_t \right). \quad (20)$$

Major difference in the effective action between the spherical and toroidal case is visible in the potential term. In the former case, the potential term is proportional to $v^{1/3}$ and is exactly the same as in the minisuperspace model. Such a term is a consequence of a constant, positive intrinsic curvature of spherical geometry and can be verified by a direct calculation of the action.

The minisuperspace model reduces degrees of freedom to the scale factor $a(t) \propto v(t)^{1/3}$, and the minisuperspace action is obtained by inserting a maximally symmetric metric,

$$\mathrm{d}s^2 = \mathrm{d}t^2 + a^2(t)\mathrm{d}\Omega^2,$$

into the (Euclidean) Einstein-Hilbert action. For a unit three-sphere, the line element in spherical coordinates is given by

$$\mathrm{d}\Omega^2 = \mathrm{d}x_2^2 + \sin^2 x_2 \mathrm{d}x_3^2 + \sin^2 x_2 \sin^2 x_3 \mathrm{d}x_4^2.$$

Calculation of the Christoffel symbols and subsequently the Riemann tensor gives the scalar curvature $R = \frac{6}{a^2}(-\dot{a}^2 - a\ddot{a} + 1)$. Integration by parts leads to the minisuperspace action,

$$S = \frac{1}{16\pi G}\int \mathrm{d}t \int \mathrm{d}\Omega \sqrt{g}(R - 2\Lambda) \propto \frac{1}{G}\int \mathrm{d}t \left(a\dot{a}^2 - \frac{\Lambda}{3}a^3 + a \right),$$

or equivalently in terms of the spatial volume observable to

$$S = \int \mathrm{d}t \left(\frac{1}{\Gamma}\frac{\dot{v}^2}{v} - \lambda v + \mu v^{1/3} \right).$$

On the other hand, for a toroidal geometry the metric is Euclidean $\mathrm{d}\Omega^2 = \mathrm{d}x_2^2 + \mathrm{d}x_3^2 + \mathrm{d}x_4^2$ and the intrinsic curvature vanishes. The scalar curvature $R = \frac{6}{a^2}(-\dot{a}^2 - a\ddot{a})$ produces the toroidal minisuperspace action:

$$S \propto \frac{1}{G}\int \mathrm{d}t \left(a\dot{a}^2 - \frac{\Lambda}{3}a^3 \right) \quad \text{thus} \quad S = \int \mathrm{d}t \left(\frac{1}{\Gamma}\frac{\dot{v}^2}{v} - \lambda v \right).$$

Lack of the classical potential term might simplify observations of quantum corrections.

IV. DISCUSSION

We used the computer generated numerical data to measure the spatial volume profile and the covariance of spatial volume fluctuations in 3 + 1-dimensional CDT with

[6]Note that in the potential part we have included a linear term $+\lambda n_t$. The term is not recorded in the measured covariance matrix data which depend on second derivatives of the effective action only. We have chosen the "+" sign (with $\lambda > 0$) based on different measurement methods which will be described in a forthcoming article.

toroidal spatial topology boundary conditions and to determine the effective action. The form of the action observed for the 3 + 1-dimensional toroidal case (20),

$$S_{\mathrm{eff}}^{(T^3)} = \sum_t \left(\frac{(n_t - n_{t+1})^2}{\Gamma(n_t + n_{t+1} - 2n_0)} + \lambda n_t + \mu n_t^{-\gamma} \right), \qquad (21)$$

with $\gamma \approx 1.16$ can be compared with the minisuperspace action of the 3 + 1-dimensional spherical case [37,38],

$$S_{\mathrm{eff}}^{(S^3)} = \sum_t \left(\frac{(n_t - n_{t+1})^2}{\Gamma(n_t + n_{t+1} - 2n_0)} - \lambda n_t + \mu n_t^{1/3} \right). \qquad (22)$$

The kinetic term present in both actions is a classical term in the sense that precisely such a term is present in the minisuperspace reduction of the Einstein-Hilbert action both for the spatial topology S^3 and T^3. Interestingly, the numerical value of the effective parameter $\Gamma \approx 26.3$ measured in the point ($\kappa_0 = 2.2$, $\Delta = 0.6$) is, up to statistical precision, identical in both cases. The potential term $\mu\, n_t^{1/3}$ in (22) is also a classical term as it is present in the minisuperspace model when the spatial topology is S^3, and it is responsible for the semiclassical S^4-like background solution observed in the computer simulations. However, such a term is not present in suitable minisuperspace reduction when the spatial topology is T^3, and we do not observe it in the computer simulations. The term we do observe, $n_t^{-\gamma}$, is numerically quite small and has the interpretation of a genuine quantum correction. The potential term is purely due to quantum corrections. It would be very interesting to calculate analytically the exponent γ.

ACKNOWLEDGMENTS

J. G. S. and J. J. wish to acknowledge the support of Grant No. DEC-2012/06/A/ST2/00389 from the National Science Centre Poland. J. A. and A. G. acknowledge support from the ERC Advanced Grant No. 291092 "Exploring the Quantum Universe" (EQU) and from FNU, the Free Danish Research Council, through the grant "Quantum Gravity and the Role of Black Holes." A. G. acknowledges support by the National Science Centre, Poland, under Grant No. 2015/17/D/ST2/03479. In addition, J. A. was supported in part by the Perimeter Institute of Theoretical Physics. Research at the Perimeter Institute is supported by the Government of Canada through Industry Canada and by the Province of Ontario through the Ministry of Economic Development and Innovation.

APPENDIX A: MINIMAL CONFIGURATION OF A THREE-TORUS

In the presented setup, spatial slices are three-dimensional simplicial manifolds of a toroidal topology build of tetrahedra. In this appendix, we investigate the smallest triangulation of a three-torus, i.e. possessing a minimal number of vertices (N_0) and tetrahedra (N_3). It is also a very interesting problem from a mathematical point of view.

By construction, CDT triangulations do not allow for distinct edges with the same endpoints. Thus, the shortest loop consists of three vertices and three links (it is a triangle). Naively, the minimal triangulation would be a Cartesian product of three such loops (one in each direction) consisting of $3^3 = 27$ points. Surprisingly, the smallest observed spatial slice has only 15 points. This is possible, because the loops in different directions interlace. The found configuration consists of $N_0 = 15$ points, $N_1 = \binom{15}{2} = 105$ links, $N_2 = 180$ triangles and $N_3 = 90$ tetrahedra. It is a good candidate for the smallest triangulation of T^3 because it has a well-defined structure, and for $N_0 = 15$, only one combination of N_1 and N_3 was observed.

1. Layered structure

The structure of the discovered minimal configuration is codified by links. The number of links N_1 saturates the upper bound for 15 points which means that each vertex is connected to the other. There are only two types of links: (i) with coordination number (order) equal to 4 and (ii) with coordination number equal to 6. Each point has identical vicinity shown in Fig. 8—8 outgoing links of order 6 and 6 outgoing links of order 4. The latter links are marked with a thick red line and define the x, y and z axis (in both

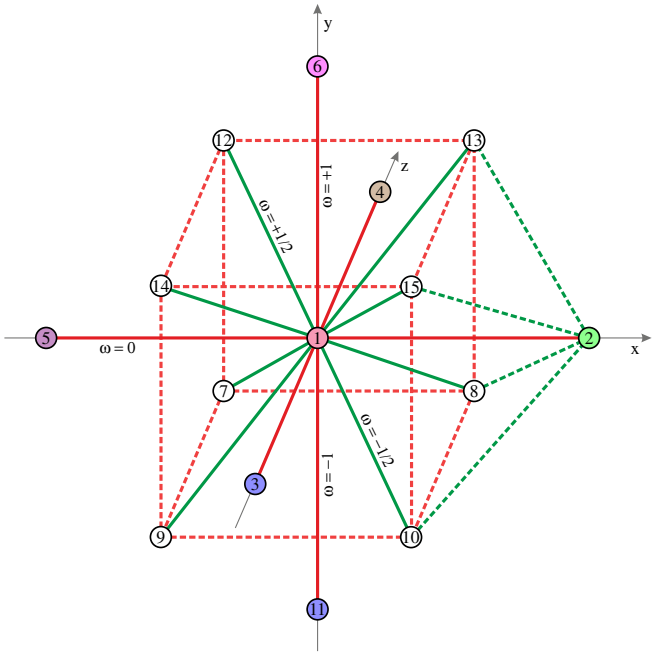

FIG. 8. Neighborhood of vertex 1. The six outgoing links of order 4 are marked with a thick red line, they determine the x, y and z directions. Vertices 2, 3, 4 and 5 lie in the same layer L_0 (x-z plane) as vertex 1. The eight outgoing links of order 6 are marked with a thick green line. The structure for each point is identical. Note that each vertex is connected to each other.

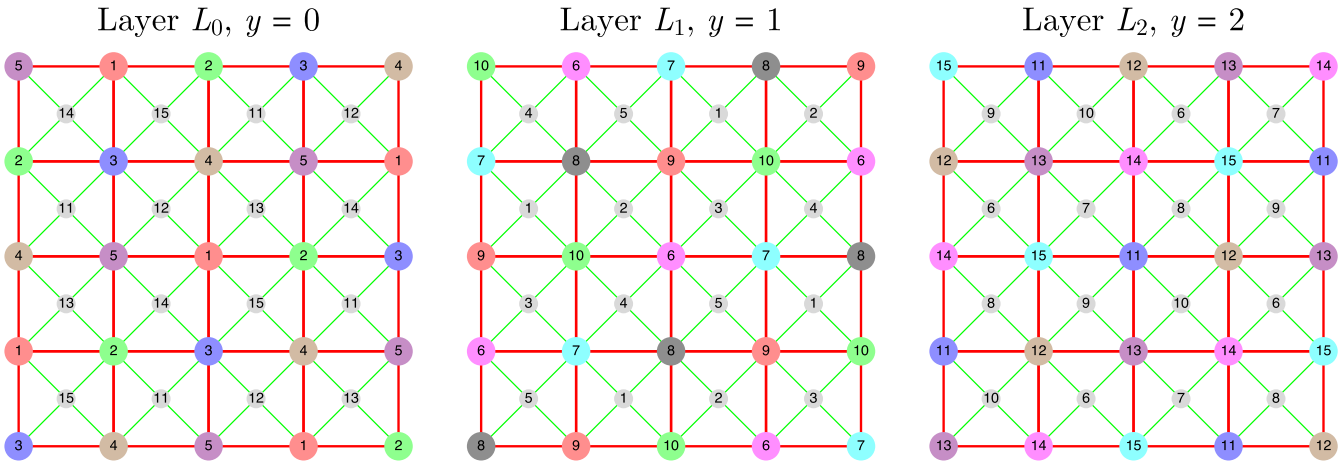

FIG. 9. Vertices of the minimal triangulation of T^3 can be divided into three disjoint layers of equal size. The layers can be viewed as x-z planes indexed by coordinate y. Red lines denote links of order 4 which connect points belonging to the same layer, while green lines denote links of order six. Links of order four which connect adjacent layers are not visible. Vertices lying in a given layer are marked with color dots. Gray dots denote vertices connected by links of order six which belong to a layer shifted by a half step in the y direction. Each layer is periodic in the x and z direction with period 5.

directions). They also introduce a notion of layers, which can be identified with the x-z planes. Each of the three layers contains 5 vertices and is enumerated by a discrete coordinate $y = 0, 1, 2$.

The layers are visualized in Fig. 9, the vertices have been relabeled so that the layers are $L_0 = \{1, 2, 3, 4, 5\}$, $L_1 = \{6, 7, 8, 9, 10\}$ and $L_2 = \{11, 12, 13, 14, 15\}$. Horizontal and vertical lines have coordination number 4 and are drawn with a red line. Taking a step to the right increases the x coordinate by 1 and the vertex label also by 1 (modulo 5), going upward by one step increases the z coordinate by 1 but the vertex label by 2 (modulo 5) so that there are no two links with the same endpoints. Each layer is periodic in x and z direction with period 5. The layers also form a structure with period 3 ($L_0 \to L_1 \to L_2 \to L_0$). One layer forms the smallest square grid with two nonequivalent and noncontractible loops. There are also lines orthogonal to the plot which connect different layers (different y). The layers visualized in Fig. 2. should be viewed as placed on top of each other, so that e.g. vertex 1 is connected to vertex 6 by a link of order 4.

However, the whole picture is more complicated. There are also links of order 6, marked with a green line in Fig. 8 and Fig. 9, which always connect different layers. They change the y coordinate by $\pm\frac{1}{2}$. The layers are interlaced in such a way, that a layer $y = +1$ (connected by links of order 4) is at the same time at $y = -1/2$ (connected by links of order 6). For example, layer L_2 is simultaneously lying two steps above L_0, one step below or half step above.

2. Proof of toroidal topology

To prove that the minimal triangulation indeed has a topology of a three-torus, we have to show that there are three noncontractible and nonequivalent loops. To demonstrate that all single winded loops can be split into three equivalence classes, we assign a weight ω to each link. Loops within one class can be continuously transformed into each other, but not between different classes. A link's weight basically corresponds to change in the y direction. Because every loop can be continuously transformed into a path consisting only of edges present in the triangulation, we restrict our considerations to such loops.

The weights are assigned according to the following rules, which are summarized in Table I. The weight of a link depends only on its coordination number, orientation and the layers it connects. Edges that connect vertices lying in the same layer have weight $\omega = 0$ (horizontal and vertical red links in Fig. 9). Links of order 4 connecting layers in an increasing order (i.e $L_0 \to L_1 \to L_2 \to L_0$) have weight $\omega = +1$, while links of order 6 connecting layers in a decreasing order (e.g. $L_0 \to L_2$) have weight $\omega = +1/2$ (diagonal green links in Fig. 9). Edges with opposite orientation have opposite weights. The weight of a path is a sum of the weights of links that build that path.

The clue to the proof is that any continuous transformation of a loop does not change its weight. It can be inferred from Fig. 8 that each tetrahedron has two links of order 4, which don't meet, and four links of order 6. An

TABLE I. Weights ω of links with given order and endpoint layers. The orientation is important.

Order	Connection	Weight
4	$L_y \to L_{y+1}$	$\omega = +1$
4	$L_y \to L_{y-1}$	$\omega = -1$
4	$L_y \to L_y$	$\omega = 0$
6	$L_y \to L_{y-1}$	$\omega = +1/2$
6	$L_y \to L_{y+1}$	$\omega = -1/2$

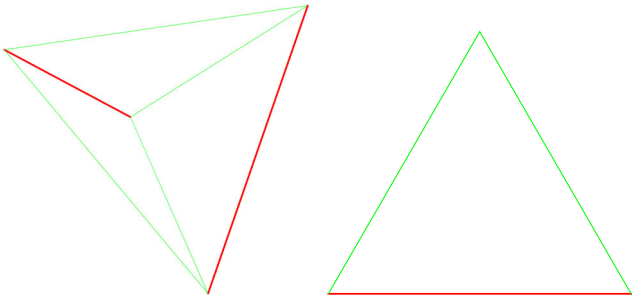

FIG. 10. The figure shows a tetrahedron and a triangle (right) present in the minimal configuration. Red line denotes a link of order 4, green line denotes a link of order 6. All tetrahedra and triangles have this form.

example of such a tetrahedron is visualized in Fig. 10 on the left. This means that every triangle consists of two links of order 6 with weight $\omega = \pm 1/2$ and one link of order 4 with weight $\omega = -1, 0, +1$. Thus every fundamental continuous transformation of a loop consists of changing one edge of a triangle into the two other or vice versa. It is easy to show that in all cases the total weight is preserved.

Case I Let the red link connect layers $L_y \to L_{y+1}$. It has a weight $\omega = +1$. Because the third point is connected by links of order 6 it cannot lie in layer L_y nor L_{y+1} and has to belong to layer L_{y+2}. Thus, the green lines connect layers $L_y \to L_{y+2}$ and $L_{y+2} \to L_{y+1}$ and both have weight $\omega = +1/2$ which gives in total $\omega = +1$.

Case II Similarly, when the red link connects points in the same layer $L_y \to L_y$ it has a weight $\omega = 0$. The third point has to be placed either in layer L_{y-1} or L_{y+1}. The green links are then $L_y \to L_{y+1}$ and $L_{y+1} \to L_y$ with total weight $\omega = -1/2 + 1/2 = 0$ or $L_y \to L_{y-1}$ and $L_{y-1} \to L_y$ with total weight $\omega = +1/2 - 1/2 = 0$.

Taking the orientation properly into account, we can prove all remaining cases (e.g. transformation of a red and a green link into a green link).

The next step is to identify the equivalence classes of loops. Let us consider the following representatives:

First loop

$$\mathbf{1}(L_0) \xrightarrow[\omega=0]{4} \mathbf{2}(L_0) \xrightarrow[\omega=0]{4} \mathbf{5}(L_0) \xrightarrow[\omega=0]{4} \mathbf{1}(L_0)$$

Numbers in bold are labels of vertices belonging to the path, in parentheses are vertex layers. Arrows denote links with endpoints on sides, the numbers above are link orders. The weight can be derived from rules in Table I. This loop is completely embedded in layer L_0 and its total weight is $\omega = \mathbf{0}$. All contractible loops of length three form a triangle present in the triangulation. Because there are no triangles composed exclusively of links of order 4, this loop is noncontractible.

Second loop

$$\mathbf{1}(L_0) \xrightarrow[\omega=1/2]{6} \mathbf{13}(L_2) \xrightarrow[\omega=1/2]{6} \mathbf{10}(L_1) \xrightarrow[\omega=1/2]{6} \mathbf{1}(L_0)$$

This loop passes through all layers in a descending order along links with coordination number 6 (weight $+1/2$). The total weight equals $\omega = \mathbf{3/2}$. Because the weight is nonzero, it cannot be a contractible loop.

Third loop

$$\mathbf{1}(L_0) \xrightarrow[\omega=1]{4} \mathbf{6}(L_1) \xrightarrow[\omega=1]{4} \mathbf{11}(L_2) \xrightarrow[\omega=1]{4} \mathbf{1}(L_0)$$

This loop passes through consecutive layers along links of order 4 (weight $+1$). The total weight equals $\omega = \mathbf{3}$, and because it is nonzero the loop is noncontractible. It is also too short to be a loop of second type winded twice.

Moreover, the foregoing loops are noncontractible because they have length three but do not form a triangle present in the simplicial manifold. Because they have different weights, they necessarily belong to separate equivalence classes. This ends the proof of toroidal topology of the considered triangulation. It is also noteworthy that the minimal toroidal triangulation consists of 90 tetrahedra, which is much more than for a spherical topology (5 tetrahedra).

[1] G. 't Hooft and M. Veltman, One loop divergencies in the theory of gravitation, in *Euclidean Quantum Gravity*, edited by G. W. Gibbons and S. W. Hawking (World Scientific, Singapore, 1993), pp. 3–28.

[2] M. H. Goroff and A. Sagnotti, The ultraviolet behavior of Einstein gravity, Nucl. Phys. **B266**, 709 (1986).

[3] S. Weinberg, Ultraviolet divergences in quantum theories of gravitation, in *General Relativity: An Einstein Centenary Survey*, edited by S. W. Hawking and W. Israel (Cambridge University Press, 1979), pp. 790–831.

[4] H. Kawai and M. Ninomiya, Renormalization group and quantum gravity, Nucl. Phys. **B336**, 115 (1990).

[5] H. Kawai, Y. Kitazawa, and M. Ninomiya, Scaling exponents in quantum gravity near two-dimensions, Nucl. Phys. **B393**, 280 (1993).

[6] M. Reuter, Nonperturbative evolution equation for quantum gravity, Phys. Rev. D **57**, 971 (1998).

[7] A. Codello, R. Percacci, and C. Rahmede, Investigating the ultraviolet properties of gravity with a Wilsonian renormalization group equation, Ann. Phys. (Amsterdam) **324**, 414 (2009).

[8] M. Reuter and F. Saueressig, Functional renormalization group equations, asymptotic safety, and quantum Einstein gravity, arXiv:0708.1317.
[9] M. Niedermaier and M. Reuter, The asymptotic safety scenario in quantum gravity, Living Rev. Relativ. **9**, 5 (2006).
[10] D. F. Litim, Fixed Points of Quantum Gravity, Phys. Rev. Lett. **92**, 201301 (2004).
[11] T. Regge, General relativity without coordinates, Nuovo Cimento **19**, 558 (1961).
[12] F. David, Planar Diagrams Two-dimensional lattice gravity and surface models, Nucl. Phys. **B257**, 45 (1985).
[13] V. A. Kazakov, A. A. Migdal, and I. K. Kostov, Critical properties of randomly triangulated planar random surfaces, Phys. Lett. B **157**, 295 (1985).
[14] D. V. Boulatov, V. A. Kazakov, I. K. Kostov, and A. A. Migdal, Analytical and numerical study of the model of dynamically triangulated random surfaces, Nucl. Phys. **B275**, 641 (1986).
[15] M. E. Agishtein and A. A. Migdal, Three-dimensional quantum gravity as dynamical triangulation, Mod. Phys. Lett. A **06**, 1863 (1991).
[16] D. V. Boulatov and A. Krzywicki, On the phase diagram of three-dimensional simplicial quantum gravity, Mod. Phys. Lett. A **06**, 3005 (1991).
[17] J. Ambjorn and S. Varsted, Three-dimensional simplicial quantum gravity, Nucl. Phys. **B373**, 557 (1992).
[18] J. Ambjorn and J. Jurkiewicz, Four-dimensional simplicial quantum gravity, Phys. Lett. B **278**, 42 (1992).
[19] M. E. Agishtein and A. A. Migdal, Simulations of four-dimensional simplicial quantum gravity, Mod. Phys. Lett. A **07**, 1039 (1992).
[20] S. Catterall, J. B. Kogut, and R. Renken, Phase structure of four-dimensional simplicial quantum gravity, Phys. Lett. B **328**, 277 (1994).
[21] J. Ambjorn, B. Durhuus, and T. Jonsson, Quantum geometry: A Statistical field theory approach, *Cambridge Monographs on Mathematical Physics* (Cambridge University Press, Cambridge, England, 1997).
[22] J. Hartle and S. Hawking, Wave function of the universe, Phys. Rev. D **28**, 2960 (1983).
[23] J. Ambjorn, L. Glaser, A. Goerlich, and J. Jurkiewicz, Euclidian 4d quantum gravity with a non-trivial measure term, J. High Energy Phys. 10 (2013) 100.
[24] D. Coumbe and J. Laiho, Exploring Euclidean dynamical triangulations with a non-trivial measure term, J. High Energy Phys. 04 (2015) 028.
[25] P. Bialas, Z. Burda, A. Krzywicki, and B. Petersson, Focusing on the fixed point of 4-D simplicial gravity, Nucl. Phys. **B472**, 293 (1996).
[26] B. V. de Bakker, Further evidence that the transition of 4-D dynamical triangulation is first order, Phys. Lett. B **389**, 238 (1996).
[27] J. Laiho, S. Bassler, D. Coumbe, D. Du, and J. T. Neelakanta, Lattice quantum gravity and asymptotic safety, arXiv:1604.02745.
[28] S. Bilke, Z. Burda, and B. Petersson, Topology in 4-D simplicial quantum gravity, Phys. Lett. B **395**, 4 (1997).
[29] A. Dasgupta and R. Loll, A proper time cure for the conformal sickness in quantum gravity, Nucl. Phys. **B606**, 357 (2001).
[30] J. Ambjorn, J. Jurkiewicz, and R. Loll, Dynamically triangulating Lorentzian quantum gravity, Nucl. Phys. **B610**, 347 (2001).
[31] J. Ambjorn, J. Jurkiewicz, and R. Loll, Reconstructing the universe, Phys. Rev. D **72**, 064014 (2005).
[32] J. Ambjorn, A. Gorlich, S. Jordan, J. Jurkiewicz, and R. Loll, CDT meets Hořava-Lifshitz gravity, Phys. Lett. B **690**, 413 (2010).
[33] J. Ambjørn, J. Gizbert-Studnicki, A. Görlich, and J. Jurkiewicz, The effective action in 4-dim CDT. The transfer matrix approach, J. High Energy Phys. 06 (2014) 034.
[34] J. Ambjørn, D. N. Coumbe, J. Gizbert-Studnicki, and J. Jurkiewicz, Signature change of the metric in CDT quantum gravity?, J. High Energy Phys. 08 (2015) 033.
[35] J. Ambjorn, J. Jurkiewicz, and R. Loll, Emergence of a 4-D World from Causal Quantum Gravity, Phys. Rev. Lett. **93**, 131301 (2004).
[36] J. Ambjorn, A. Gorlich, J. Jurkiewicz, and R. Loll, Planckian Birth of the Quantum de Sitter Universe, Phys. Rev. Lett. **100**, 091304 (2008).
[37] J. Ambjorn, A. Gorlich, J. Jurkiewicz, and R. Loll, The nonperturbative quantum de Sitter universe, Phys. Rev. D **78**, 063544 (2008).
[38] J. Ambjørn, A. Görlich, J. Jurkiewicz, R. Loll, J. Gizbert-Studnicki, and T. Trześniewski, The semiclassical limit of causal dynamical triangulations, Nucl. Phys. **B849**, 144 (2011).
[39] J. Ambjorn, S. Jordan, J. Jurkiewicz, and R. Loll, A Second-Order Phase Transition in CDT, Phys. Rev. Lett. **107**, 211303 (2011).
[40] J. Ambjorn, S. Jordan, J. Jurkiewicz, and R. Loll, Second- and first-order phase transitions in CDT, Phys. Rev. D **85**, 124044 (2012).
[41] D. N. Coumbe, J. Gizbert-Studnicki, and J. Jurkiewicz, Exploring the new phase transition of CDT, J. High Energy Phys. 02 (2016) 144.
[42] J. Ambjorn, A. Goerlich, J. Jurkiewicz, A. Kreienbuehl, and R. Loll, Renormalization group flow in CDT, Classical Quantum Gravity **31**, 165003 (2014).
[43] J. Ambjorn, D. Coumbe, J. Gizbert-Studnicki, and J. Jurkiewicz, Searching for a continuum limit in causal dynamical triangulation quantum gravity, Phys. Rev. D **93**, 104032 (2016).
[44] P. S. Mara, Triangulations for the cube, J. Comb. Theory Ser. A **20**, 170 (1976).